Optics Letters

Dual-wavelength distributed feedback laser array based on four-phase-shifted sampled Bragg grating for terahertz generation

Yizhe Fan,* Bocheng Yuan, Mohanad Al-Rubaiee, Yiming Sun, Simeng Zhu, John H. Marsh, and Lianping Hou

James Watt School of Engineering, University of Glasgow, Glasgow G12 8QQ, UK
**2636405F@student.gla.ac.uk*

Received 18 March 2024; revised 13 May 2024; accepted 28 May 2024; posted 28 May 2024; published 12 June 2024

We propose and experimentally demonstrate a dual-wavelength distributed feedback (DFB) laser array utilizing a four-phase-shifted sampled Bragg grating. By using this grating, the coupling coefficient is enhanced by approximately 2.83 times compared to conventional sampled Bragg gratings. The devices exhibit a stable dual-mode lasing achieved by introducing further π-phase shifts at 1/3 and 2/3 positions along the cavity. These devices require only one stage of lithography to define both the ridge waveguide and the gratings, mitigating issues related to misalignment between them. A dual-wavelength laser array has been fabricated with frequency spacings of 320 GHz, 500 GHz, 640 GHz, 800 GHz, and 1 THz. When integrated with semiconductor optical amplifiers, the output power of the device can reach 23.6 mW. Furthermore, the dual-wavelength lasing is maintained across a wide range of injection currents, with a power difference of <3 dB between the two primary modes. A terahertz (THz) signal has been generated through photomixing in a photoconductive antenna, with the measured power reaching 12.8 μW.

https://doi.org/10.1364/OL.524107

Terahertz (THz) frequency sources have garnered significant interest owing to their wide-ranging applications in environmental detection, bio-imaging, sensing, and communications [1,2]. Researchers have explored various methods, encompassing both electrical and optical approaches, for THz generation [3–5]. The all-optical method involves the use of nonlinear crystals for optical mixing to generate THz signals and requires complex collimation systems. An optimal optical approach for THz generation is photomixing, utilizing a photoconductive antenna (PCA), where two distinct longitudinal modes are mixed to produce a time-varying current and electromagnetic field. Compared to employing discrete laser sources, the use of monolithically integrated dual-wavelength lasers (DWLs) simplifies the collimation and polarization system. Additionally, DWLs demonstrate similar mode-noise rejection effects for the two longitudinal modes, enhancing their phase correlation.

Distributed feedback lasers (DFBs) determine the lasing wavelength through periodic grating structures. DWLs utilizing uniform Bragg gratings have been reported to have the capability to generate THz signals [6]. However, the resolution limitations of electron beam lithography (EBL) restrict the difference in the corrugation pitch to no less than 0.5 nm, thereby placing a lower limit on the frequency difference between the two longitudinal modes [7]. To overcome the constraints imposed by EBL on high-precision wavelength control, an effective approach is the reconstruction-equivalent-chirp (REC) technique, which employs sampled Bragg gratings (SBGs) [8]. In REC, a constant seed grating period defines a center wavelength, with aperiodic SBG section enabling precise control of the wavelength of the side modes.

Conventional sampled Bragg gratings (C-SBGs) have been commonly employed in REC designs [9,10], where each sampling period comprises half with a seed grating and half without. However, the coupling coefficient, κ, of the ±first-order side modes of a C-SBG is only $1/\pi$ times that of a uniform Bragg grating (UBG) [11], and for a device lasing on the +first-order channel, the presence of the zeroth and –first channels can negatively impact laser performance. As a result, DFB lasers utilizing two-phase-shifted sampled Bragg gratings (2PS-SBGs) have been used in fabricating arrays with a wavelength spacing of around 0.8 nm [12]. This structure featured two sections within each sampling period, with each section having a length equal to half the sampling period and a π-phase shift difference between them. In the 2PS-SBG, the zeroth-order mode is suppressed and the +first channel reflections were used as the lasing channels. The utilization of both −first- and +first-order channels for generating a DWL to generate 560 GHz signals has also been reported [13]. However, achieving smaller channel spacing requires a considerable increase in the sampling period due to their inverse proportionality relationship. For instance, a 320 GHz DWL at 1.55 μm based on the 2PS-SBG typically necessitates a sampling period exceeding 300 μm [14].

Here, we present a semiconductor DWL array based on a four-phase-shifted sampled Bragg grating (4PS-SBG) and a sidewall grating structure. The device incorporates a sidewall

Table 1. Parameters for the DWL Array

Channel	P_1 (nm)	P_2 (nm)	Designed Frequency
CH1	4639	4806	320 GHz
CH2	4639	4906	500 GHz
CH3	4639	4986	640 GHz
CH4	4639	5082	800 GHz
CH5	4639	5206	1 THz

grating structure, with each side featuring a distinct sampling period. The +first-order reflections are used resulting in the generation of two lasing modes, and the wavelength separation between these modes is regulated by varying the sampling periods. The 4PS-SBG exhibits a higher effective κ (0.9 times that of a UBG) compared to the 2PS-SBG (0.64 times that of a UBG). This enhancement, coupled with the elimination of the zeroth channel subgrating reflection, helps avoid negative effects from unwanted longitudinal modes. To ensure a single longitudinal mode (SLM) operation of each mode, an additional π-phase shift section is introduced in the cavity. To mitigate mode competition between the two longitudinal modes, these phase shifts are strategically positioned at 1/3 of the cavity for one mode and 2/3 of the cavity for the other. In comparison to traditional buried DWL gratings, our approach utilizing a sidewall grating structure can be defined through a streamlined fabrication process involving only one step of metal organic chemical vapor deposition (MOCVD) and one step of III–V material etching.

In this Letter, we demonstrate a DWL array with frequency spacings of 320 GHz, 500 GHz, 640 GHz, 800 GHz, and 1 THz, based on the 4PS-SBG architecture. A stable and uniform intensity dual-wavelength lasing can be maintained over a wide range of DFB injection current and electroabsorption modulator (EAM) reverse voltage settings, as confirmed by both the measured optical spectra and autocorrelation traces. Each device in the array has been used to generate a THz signal using a PCA, with the 500 GHz DWL device providing a THz signal power of approximately 12.8 μW.

The key issue in designing DWL is to use two different +first-order channels and each of them represents a single-mode operation. The wavelength of the +first-order subgrating λ_{+1} can be expressed as follows [15]:

$$\lambda_{+1} = 2n_{\text{eff}}\frac{P\Lambda_0}{P+\Lambda_0}, \tag{1}$$

where n_{eff} denotes the effective refractive index of the ridge waveguide, while P represents the sampling period, and Λ_0 indicates the seed grating period. The ridge waveguide exhibits an effective refractive index n_{eff} of 3.19. The seed grating period Λ_0 is set to 257 nm, corresponding to a wavelength of 1630 nm at the zeroth channel. The sampling periods are precisely adjusted to position the +first-order sub-grating channel around 1555 nm, aligning with the gain peak of the multiple quantum well (MQW) material. It is crucial to consider the dispersion coefficient, measured at −0.00021/nm, when determining the sampling periods (P_1 and P_2) for the two lasing modes. For all five DWLs, P_1 is set to 4639 nm. The specific P_2 for the five DWLs are detailed in Table 1.

The DWLs are constructed using the AlGaInAs-/InP-based material system. Its MQW structure comprises five quantum wells (QWs) and six quantum barriers (QBs). Each QW measures 6 nm in thickness with a compressive strain of 1.2%, while the QB has a thickness of 10 nm with a tensile strain of −0.3% [16].

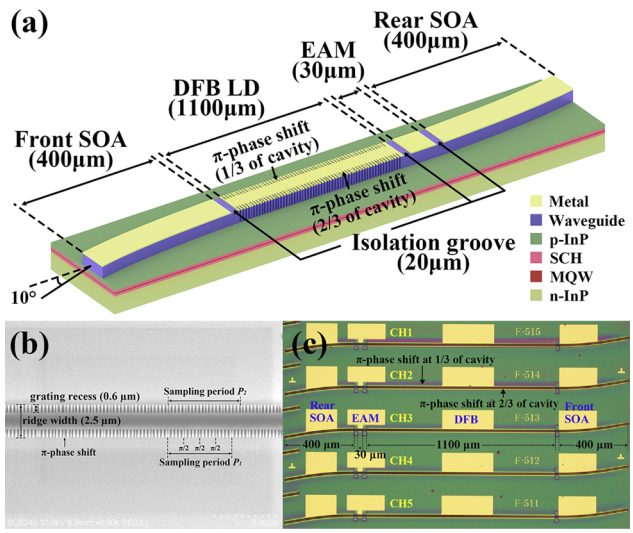

Fig. 1. (a) Schematic of the dual-wavelength DFB laser based on 4PS-SBG. (b) SEM image of the ridge waveguide and sidewall grating defined by HSQ. (c) Optical microscopic picture of the device.

The schematic of the device is illustrated in Fig. 1(a). The DWL features an 1100-μm-long DFB section using two 4PS-SBGs [12,15].

Two semiconductor optical amplifiers (SOAs), each measuring 400 μm in length, are positioned at the front and rear sides, offering gain equalization. Adjustment of the SOA current enables slight alterations in the photon distribution within the DFB laser cavity. The curved waveguides (with a radius of 1730 μm) of the SOAs are designed to produce a 10° angled output facet resulting in an intensity reflectivity around 10^{-4} at 1550 nm, thereby minimizing the occurrence of Fabry–Perot (FP) modes induced by facet reflection. Within the DFB laser cavity, π-phase shift sections are inserted at 1/3 and 2/3 of the DFB cavity length respectively on either side of the ridge waveguide. This configuration enables each side to operate in a SLM at the intended wavelength. Given that the photon density peaks occur around the π-phase-shifted sections [17], distributing these sections across the DFB laser cavity separates the positions of peak light intensities of the two lasing modes. As a result, this configuration mitigates mode competition, ensuring a stable dual longitudinal mode operation across a wide range of operating currents [7]. The EAM section, spanning 30 μm in length, enhances the phase relationship between the two lasing modes and stabilizes the mode beating frequency through the mechanism of four-wave mixing (FWM) [18]. Each section is isolated by a 20-μm-long electrical isolation, achieved through etching the heavily doped 200-nm-thick InGaAs contact layer and the 50 nm 1.3Q layer. This isolation results in a corresponding resistance of approximately 10 kΩ.

Figure 1(b) shows the hydrogen silsesquioxane (HSQ) grating mask before the dry etching process. The ridge waveguide is 2.5 μm wide, with grating recesses measuring 0.6 μm on both sides of the ridge. Figure 1(c) is a microscopic image of the DWL array, while the sampling periods and frequency spacings for each sidewall are detailed in Table 1. The measured effective κ of the DWL array is approximately 10 cm^{-1}. The ratio

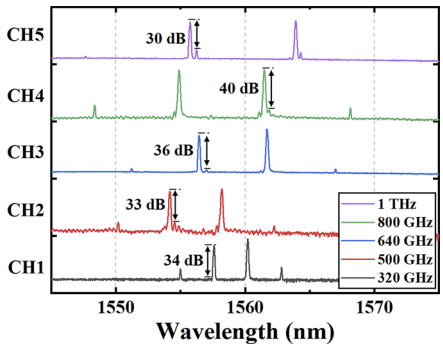

Fig. 2. Measured optical spectrum for each DWL device.

Table 2. Measurement Conditions for the DWL Array

Channel	Designed Frequency	I_{R-SOA} (mA)	V_{EAM} (V)	I_{DFB} (mA)	I_{F-SOA} (mA)
CH1	320 GHz	35	−1.5	295	40
CH2	500 GHz	0	0	195	60
CH3	640 GHz	0	0	175	40
CH4	800 GHz	0	−1.2	295	60
CH5	1 THz	0	0	105	40

between the effective κ of the 4PS-SBG and that of the UBG is approximately 0.83, slightly below the theoretical value of 0.9 [15]. This deviation is likely attributed to the reactive ion etching (RIE) lag effect encountered during the sidewall grating fabrication process [19].

The fabricated devices were mounted with the epitaxial layer facing up on a copper heat sink using indium. A thermoelectric cooler supplemented by water cooling was used to control the temperature of the copper heat sink. All measurements were conducted under continuous-wave conditions at 20°C, collecting light from the front SOA. The devices had a typical threshold current of 60 mA and the maximum output power could reach 23.6 mW at a DFB current (I_{DFB}) of 280 mA and a front SOA current (I_{F-SOA}) of 80 mA. The comparatively lower output power may result from the misalignment between the peak gain of the front SOA (1520 nm) at 60 mA and the center wavelength of the DWL, which is more than 1556 nm. Addressing this issue can be achieved by optimizing the length of the SOA.

The measured optical spectra of the five DWL devices, along with their designed frequency spacings, are presented in Fig. 2. Table 2 outlines the measurement conditions for each device. Notably, the DWLs exhibit favorable phase relationships between the two primary lasing modes, with observable FWM signals. The side mode suppression ratios (SMSRs) for each device exceed 30 dB, while the power differences between the two main modes (PDM) are less than 3 dB. In the scanning optical spectra 2D map (320 GHz, 640 GHz, 800 GHz, and 1 THz) depicted in Fig. 3, the devices demonstrate a dual-mode lasing across a DFB current range exceeding 40 mA. As the DFB current increases, the spacing between the two lasing modes remains constant, ensuring a stable beat tone. However, occasional mode hopping is observed in the 320 GHz and 1 THz DWLs, possibly attributable to random phase shifts introduced from the cleaved SOA facets. I_{R-SOA} of 35 mA is chosen for CH1 to achieve relatively uniform gain for the two lasing wavelengths. Conversely, the I_{R-SOA} for CH2 to CH5 is kept at 0 mA to ensure

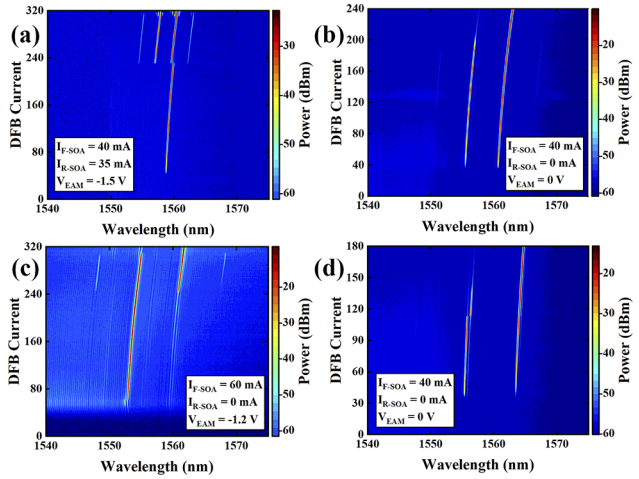

Fig. 3. 2D optical spectra map of the DWL devices at different frequency spacings: (a) 320 GHz, (b) 640 GHz, (c) 800 GHz, and (d) 1 THz.

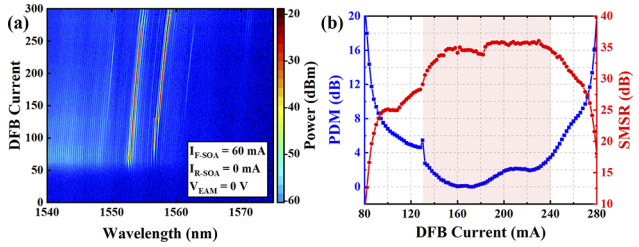

Fig. 4. (a) 2D optical spectra map and (b) SMSR and PDM as a function of the DFB current for the 500 GHz DWL device.

uniform gain while suppressing reflection from the rear SOA. Utilizing additional anti-reflection (AR) coatings on the SOA facet with less than 1×10^{-5} reflection reduces the influence of external feedback into the SOA, thus expecting relatively less mode hopping [20].

In Fig. 4(a), we present a 2D optical spectrum map for the CH2 DWL (500 GHz). The device demonstrates a stable dual-mode lasing behavior with a frequency spacing of 500 GHz within the I_{DFB} range of 130–240 mA, with $I_{F-SOA} = 60$ mA, $I_{R-SOA} = 0$ mA, and $V_{EAM} = 0$ V. The spectra reveal the presence of a FWM signal under these operating conditions. When I_{DFB} exceeds the threshold current ($I_{DFB} \geq 60$ mA) but remains below 130 mA, the device exhibits some mode hopping, resulting in a dual-wavelength frequency spacing of 450 GHz. The power difference between the two modes (PDM) and the side mode suppression ratio (SMSR) are depicted in Fig. 4(b). Within the dual-mode lasing range (I_{DFB} from 130 to 240 mA), the PDM remains less than 3 dB, and the SMSR exceeds 32 dB. The sudden jump observed at an I_{DFB} of 130 mA is attributed to the mode hopping, as illustrated in Fig. 4(a).

Figure 5 shows the measured autocorrelation (AC) traces of the five DWL devices. The laser output signal containing two SLMs was amplified by an erbium-doped fiber amplifier (EDFA) and transmitted into the autocorrelator for time-domain analysis. The reciprocal of the average autocorrelation trace period of each DWL is consistent with its frequency separation measured in the optical spectra in Fig. 2, which indicates a relatively stable phase relationship between the two SLMs.

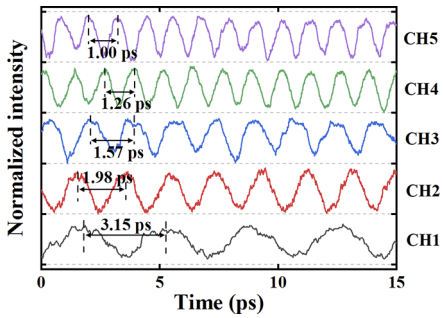

Fig. 5. Normalized AC trace measured for each DWL device.

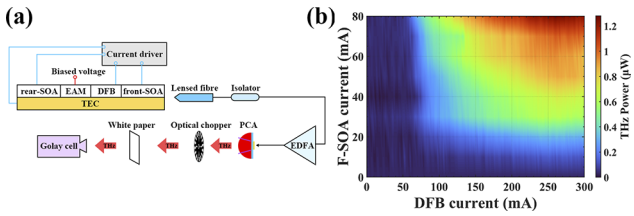

Fig. 6. (a) Setup for THz measurement. (b) Measured THz power as a function of I_{DFB} and I_{F-SOA} when I_{R-SOA} is at 0 mA.

Figure 6(a) is a schematic of the experimental setup for the generation and detection of THz signals. The output light emitted by the DWL was initially coupled into a lensed fiber, subsequently passing through an optical isolator. The light was amplified by an EDFA and was injected into the PCA to generate THz signals via the photomixing effect. The output signal from the DWL was amplified to an average power of 25 mW maintaining it just below the maximum power specified for the PCA. The PCA operated with a bias voltage of 8 V. The resulting THz waves were then directed into a Golay cell for signal power detection. To extract the small THz signal from the ambient noise, an optical chopper, operating at a modulation frequency of 20 Hz, was employed after the PCA. It is worth noting that during the experiment, a piece of white paper with a density of 80 g/m^2 was inserted between the optical chopper and the Golay cell. This was done to block the transmission of any 1.55 μm light passing through the PCA while still effectively allowing the THz signal to pass through [21]. Because the transmission of 1.55 μm radiation through the paper is less than 10%, confirming that the leakage of 1.55 μm laser radiation could not be responsible for more than a small fraction of the signal detected by the Golay cell. Figure 6(b) shows a 2D intensity map of the THz signal transmitted through the paper, acquired from the CH2 laser with 500 GHz frequency spacing. The signal power below the threshold current is considered as the noise level and has been subtracted. The device exhibits a dual-mode lasing as I_{DFB} varies from 130 to 240 mA. Notably, the power of the associated THz signal can reach 1.28 μW when I_{DFB} is set to 240 mA and I_{F-SOA} is adjusted to 80 mA, ensuring that the input power into the PCA does not exceed 25 mW. Approximately 10% of the THz signal was captured by the Golay cell, influenced by several factors: the 30° divergence angle of radiation from the PCA, the distance (140 mm) between the PCA and the entrance of the Golay cell detector, and the 11 mm diameter of the entrance cone of the detector. Considering these factors, the total estimated THz output power is approximately 12.8 μW.

In summary, we have introduced a DWL array built upon the 4PS-SBG platform, offering frequency spacings of 320 GHz, 500 GHz, 640 GHz, 800 GHz, and 1 THz. The sidewall grating structure demonstrates simplicity in fabrication, requiring only a single step of MOCVD and a solitary step of III–V dry etching. The integration of the 4PS-SBG enhances the coupling coefficient and facilitates precise control of the wavelength spacing. The lasers exhibit a stable dual-mode operation within a maximum current range of 110 mA, with a SMSR exceeding 30 dB and a PDM lower than 3 dB. Autocorrelation traces closely align with the designed frequency spacings. Additionally, the THz signal generated by PCA reaches a power level of 12.8 μW. These experimental results highlight the potential of these devices as highly integrated, user-friendly sources of terahertz radiation.

Funding. Engineering and Physical Sciences Research Council (EP/R042578/1).

Acknowledgment. We would like to acknowledge the staff of the James Watt Nanofabrication Centre at the University of Glasgow for their help in fabricating the devices.

Disclosures. The authors declare no conflicts of interest.

Data availability. Data underlying the results presented in this Letter are not publicly available at this time but may be obtained from the authors upon reasonable request.

REFERENCES

1. M. Tonouchi, Nat. Photonics **1**, 97 (2007).
2. I. Hosako, N. Sekine, M. Patrashin, *et al.*, Proc. IEEE **95**, 1611 (2007).
3. I. V. Oladyshkin, D. A. Fadeev, and V. A. Mironov, J. Opt. **17**, 075502 (2015).
4. G. M. H. Knippels, X. Yan, A. M. MacLeod, *et al.*, Phys. Rev. Lett. **83**, 1578 (1999).
5. D. Saeedkia and S. Safavi-Naeini, J. Lightwave Technol. **26**, 2409 (2008).
6. L. Hou, M. Haji, I. Eddie, *et al.*, Opt. Lett. **40**, 182 (2015).
7. Y. Fan, B. Yuan, S. Ye, *et al.*, in *IEEE Photonics Conference (IPC)*, 2022, pp. 1–2.
8. J. Li, H. Wang, X. Chen, *et al.*, Opt. Express **17**, 5240 (2009).
9. B. Yuan, S. Ye, Y. Zhang, *et al.*, in *IEEE Photonics Conference (IPC)*, 2022, pp. 1–2.
10. W. Qi, B. Yuan, J. Shi, *et al.*, in *Conference on Lasers and Electro-Optics Europe and European Quantum Electronics Conference (CLEO/Europe-EQEC)*, 2021, paper 1.
11. J. Li, Y. Cheng, Z. Yin, *et al.*, IEEE Photonics Technol. Lett. **21**, 1639 (2009).
12. S. Tang, L. Hou, X. Chen, *et al.*, Opt. Lett. **42**, 1800 (2017).
13. S. Tang, B. Hou, S. Liang, *et al.*, in *Conference on Lasers and Electro-Optics Pacific Rim (CLEO-PR)*, 2018, pp. 1–2.
14. M. Ibsen, M. K. Durkin, M. J. Cole, *et al.*, IEEE Photonics Technol. Lett. **10**, 842 (1998).
15. Y. Sun, B. Yuan, X. Sun, *et al.*, Opt. Lett. **47**, 6237 (2022).
16. L. Hou, P. Stolarz, J. Javaloyes, *et al.*, IEEE Photonics Technol. Lett. **21**, 1731 (2009).
17. J. Hong, W.-P. Huang, and T. Makino, IEEE J. Quantum Electron. **31**, 49 (1995).
18. T. Mori and H. Kawaguchi, Appl. Phys. Lett. **85**, 869 (2004).
19. S. Guilet, S. Bouchoule, C. Jany, *et al.*, in *International Conference on Indium Phosphide and Related Materials Conference*, 2006, pp. 262–265.
20. T. Kimoto, T. Kurobe, K. Muranushi, *et al.*, IEEE J. Select. Topics Quantum Electron. **11**, 919 (2005).
21. L. Hou, S. Tang, B. Hou, *et al.*, IET Optoelectron. **14**, 136 (2020).